

Computational investigation on dynamics of atmospheric pressure air discharge excited by a twin needle-plate electrode configuration

Chang-Shuo Lv(吕长硕), Wen Yan(晏雯), Zhen-Hua Bi(毕振华), Ying Song(宋颖), Jin-Hai Niu(牛金海), and De-Zhen Wang(王德真)

Citation: Chin. Phys. B, 2026, 35 (**7**): 075101. DOI: 10.1088/1674-1056/ae1cb4
http://cpb.iphy.ac.cn; http://iopscience.iop.org/cpb

What follows is a list of articles you may be interested in

Study on the interaction and evolution of surface dielectric barrier discharge channels

Hui Jiang(姜慧), Jinyu Tang(唐金宇), and Yufei Han(韩雨菲)
Chin. Phys. B, 2026, 35 (**3**): 035101. DOI: 10.1088/1674-1056/adf82b

Development characteristics of dielectric barrier discharge channels with rotating high-voltage electrodes

Hui Jiang(姜慧), Jinyu Tang(唐金宇), and Yufei Han(韩雨菲)
Chin. Phys. B, 2025, 34 (**6**): 065101. DOI: 10.1088/1674-1056/adc670

Plasma simulation to analyze velocity distribution characteristics of pseudospark-sourced electron beam

Hai-Long Li(李海龙)†, Chen-Fei Hu(胡陈飞), Che Xu(徐彻), Yong Yin(殷勇), Bin Wang(王彬), Lin Meng(蒙林), and Mao-Yan Wang(王茂琰)
Chin. Phys. B, 2020, 29 (**10**): 105101. DOI: 10.1088/1674-1056/aba274

Effect of aperture field distribution on the maximum radiated power at atmospheric pressure

Pengcheng Zhao(赵朋程), Lixin Guo(郭立新)
Chin. Phys. B, 2017, 26 (**11**): 115101. DOI: 10.1088/1674-1056/26/11/115101

Effect of electrical discharge in water on concentration of nitrate solution

F Sohbatzadeh, H Bagheri, R Safari
Chin. Phys. B, 2017, 26 (**2**): 025101. DOI: 10.1088/1674-1056/26/2/025101

Computational investigation on dynamics of atmospheric pressure air discharge excited by a twin needle-plate electrode configuration

Chang-Shuo Lv(吕长硕)[1], Wen Yan(晏雯)[1,†], Zhen-Hua Bi(毕振华)[1], Ying Song(宋颖)[1], Jin-Hai Niu(牛金海)[1], and De-Zhen Wang(王德真)[2]

[1] *Liaoning Key Laboratory of Plasma Technology, School of Physics and Materials Engineering, Dalian Nationalities University, Dalian* 116600, *China*
[2] *School of Physics, Dalian University of Technology, Dalian* 116024, *China*

(Received 19 August 2025; revised manuscript received 28 October 2025; accepted manuscript online 7 November 2025)

The large-scale low temperature plasma produced by atmospheric pressure discharge utilizing an array needle-plate electrode design has promising future applications in a variety of industries. Improving the scale and uniformity of plasma requires a thorough investigation of the interactions between needle discharges. For that purpose, a two-dimensional (2D) computational analysis of the interaction of two concurrently propagating air discharges created by a twin needle-plate electrode design is presented in the paper. Investigations are also conducted on the effect of needle spacing, pulsed peak voltage, and pulse polarity. Immediately after ignition, two identical discharges move in the same direction toward the plane electrode. The propagation route is a curve with tight needle-to-needle spacing, which is ascribed to competition between electrostatic repulsion and photoionization-induced attraction. Larger needle spacing, higher peak voltage, or negative polarity all can increase the plasma area on the plate electrode. Additionally, reducing the distance between needles or raising the pulsed peak voltage is an effective way to improve the spatial homogeneity of the discharge array. Positive voltage pulses cause a more homogeneous discharge than negative voltage pulses.

Keywords: atmospheric pressure air discharge, interaction, spatial homogeneity, fluid model

PACS: 51.50.+v, 52.25.–b, 52.40.–w, 52.65.Kj

DOI: 10.1088/1674-1056/ae1cb4 **CSTR:** 32038.14.CPB.ae1cb4

1. Introduction

Non-equilibrium atmospheric pressure plasmas have received growing interest as a result of their successful performance in a variety of present and prospective applications spanning from material surface modification and processing, water purification to sterilization and disinfection.[1–4] Various types of plasma discharge systems have been devised and explored, including dielectric barrier discharges with parallel electrodes,[5] low temperature atmospheric pressure plasma jets,[6] non-thermal plasmas with liquids.[7] Discharges with the needle electrode stand out because they can produce non-thermal plasma with lower breakdown voltage. Additionally, the use of the needle electrode can prevent the transition from the streamer to filamentary discharge, making uniform discharge easier to implement.[8]

Nevertheless, the small-scale spatial discharge structure ($\sim$ mm) with a needle electrode restricts its applications in large-scale treatments. Obtaining plasma with a broader discharge area becomes a critical topic with practical implications. In experiments, several needles have been arranged in one-dimensional (1D) or 2D arrays to expand the treatment area using plasma. It has been established that a steady and diffuse broad-area discharge plasma can be obtained by utilizing needle-array electrodes.[9–11] Researchers are increasingly concerned about how to improve the spatial homogeneity of the discharge array. For instance, Shao Tao *et al.*[12] investigated, by a combination of simulation and experiment, the spatial homogeneity of diffuse discharges produced by needle-array electrodes. Their findings imply that a more uniform discharge can be created by shortening the discharge gap between the needle in the middle of the array and the grounded electrode.

A thorough understanding of the mechanism and dynamic behaviors of discharge with the needle-array electrodes is helpful to improve discharge uniformity. Despite its importance, experimental diagnosis of needle-array discharges faces significant challenges in directly observing key physical processes. The ultrafast and stochastic nature of streamer propagation makes it extremely difficult to capture the detailed, high-resolution spatiotemporal evolution of parameters such as the spatial charge distribution and electric field enhancement around the discharge front. Furthermore, discharge uniformity is determined by the complex interplay of electrostatic repulsion and photoionization attraction between adjacent channels. These multi-physics interactions occur within microscale dimensions and on nanosecond timescales, which present a formidable challenge for experimentalists to isolate and measure individual effects without disturbing the system. In this context, numerical simulation emerges not merely as

[†]Corresponding author. E-mail: yanwen@dlnu.edu.cn

© 2026 Chinese Physical Society and IOP Publishing Ltd. All rights, including for text and data mining, AI training, and similar technologies, are reserved.

an alternative but as a crucial approach that can reveal physical details difficult to capture experimentally. This method enables researchers to systematically control key parameters while obtaining complete internal field information without interfering with the discharge process. By using a quasi-2D fluid model, Naidis[13] studied the effect of electrostatic interaction with positive streamers in atmospheric air on streamer velocity. According to the three-dimensional (3D) computational study of Luque *et al.*,[14] there are two opposing processes by which nearby discharges can interact: electrostatic repulsion of streamer heads and attraction owing to photoionization. Bourdon *et al.*[15] have conducted a numerical analysis of the merging condition for two air discharges that are propagating simultaneously under either a positive or negative polarity pulse. The ratio of the typical width of the discharge fronts to the distance between the two filaments determines whether the discharges combine or not. Zhang *et al.*[16] also investigated plasma discharge produced by needle-array electrodes with a 2D fluid model, paying attention to the influence of the factors on the discharge behaviors and plasma uniformity.

Despite significant progress in developing a complete knowledge of the discharge with needle array electrodes, the basic physics underlying the discharge is still an open question. In this work, a 2D plasma fluid model including photoionization based on three-exponential Helmholtz model is developed through the software COMSOL Multiphysics. The discharge dynamic of air plasma at atmospheric pressure generated by a twin needle-plate electrode configuration is numerically studied, aiming to provide in-depth understandings about the influencing factors dependence of discharge behaviors and spatial uniformity.

2. Model description

The discharge arrangement illustrated in Fig. 1 is employed, which is comparable to the experiment depicted in Ref. [17]. The needle electrodes are positioned along the x axis and have a height of 2 mm and a tip diameter of 0.5 mm. The y axis is generally pointed to the grounded plate. The discharge gap distance between the needle tip and the grounded electrode is set at 3 mm. A 15-kV amplitude dc pulsed high voltage is supplied to all needle electrodes simultaneously.

The discharge development process is described by a fluid model developed with the plasma module of COMSOL Multiphysics. The electron properties in this model are determined by the continuity Eq. (1) with the drift-diffusion approximation Eq. (2):[18,19]

$$\frac{\partial}{\partial t}(n_{\mathrm{e}}) + \nabla \cdot \boldsymbol{\Gamma}_{\mathrm{e}} = S_{\mathrm{e}} + S_{\mathrm{ph}}, \tag{1}$$

$$\boldsymbol{\Gamma}_{\mathrm{e}} = -(\mu_{\mathrm{e}} \cdot \boldsymbol{E})\, n_{\mathrm{e}} - D_{\mathrm{e}} \nabla n_{\mathrm{e}}, \tag{2}$$

where n_{e} represents the electron density, $\boldsymbol{\Gamma}_{\mathrm{e}}$ represents the electron flux, S_{e} and S_{ph} are the source terms of electron direct impact ionization and non-local photoionization, respectively. μ_{e} and D_{e} are the mobility and diffusion coefficients for electrons, respectively. $\boldsymbol{E}$ is the electric field. The ion transport property is given by multi-component transport equation

$$\rho \frac{\partial}{\partial t}(w_i) = \nabla \cdot \boldsymbol{\Gamma}_i = \nabla \cdot (\rho w_i \boldsymbol{V}_i) + S_{\mathrm{i}} + S_{\mathrm{ph}}, \tag{3}$$

where ρ is the mixed gas density, w_i is the mass fraction of species, $\boldsymbol{\Gamma}_i$ denotes the flux of the i-th heavy species. S_{i} is the source term of ion production by electron direct impact ionization process, $\boldsymbol{V}_i$ is the multi-component diffusion velocity. The definition of $\boldsymbol{V}_i$ depends on the option chosen for the Diffusion Model property. In this work, Mixture Averaged is chosen. The multi-component diffusion velocity is defined as

$$\boldsymbol{V}_i = D_{i,m} \frac{\nabla w_i}{w_i} + D_{i,m} \frac{\nabla M_n}{M_n} - z_i \mu_{i,m} \boldsymbol{E}, \tag{4}$$

where $D_{i,m}$ is the mixture averaged diffusion coefficient, M_n is the mean molar mass of the mixture, z_i is the charge number and $\mu_{i,m}$ is the mixture averaged mobility.

The electric potential is computed by solving Poisson's equation

$$\nabla^2 \boldsymbol{\Phi} = -\frac{\rho}{\varepsilon_0}, \tag{5}$$

where the physical constant ε_0 is the permittivity of vacuum, and ρ is a space charge density. Under static conditions, the electric field is defined by the relationship $\boldsymbol{E} = -\nabla \boldsymbol{\Phi}$. The boundary conditions of the plasma dynamics model are summarized in Table 1.

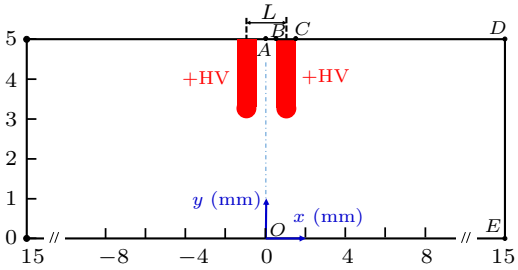


Fig. 1. The discharge configuration used in the simulation.

Table 1. Boundary conditions used for the plasma dynamics model. Needle is the high voltage electrode. Φ_{a} is the applied voltage. The boundaries AB, CD, *etc.*, are given in Fig. 1.

	AO, DE	Needle	AB, CD	EO
n_{e}	$\frac{\partial n_{\mathrm{e}}}{\partial x} = 0$	wall	$-\boldsymbol{n} \cdot \boldsymbol{\Gamma}_{\mathrm{e}} = 0$	wall
n_i	$\frac{\partial n_i}{\partial x} = 0$	wall	$-\boldsymbol{n} \cdot \boldsymbol{\Gamma}_i = 0$	wall
$\boldsymbol{\Phi}$	$\frac{\partial \boldsymbol{\Phi}}{\partial x} = 0$	Φ_{a}	$\frac{\partial \boldsymbol{\Phi}}{\partial y} = 0$	0

The working gas is dry air at room temperature and one bar (1 bar = 10^5 Pa) pressure. The charged species included in the model are positive ions, negative ions, and electrons.

A simplified chemistry mechanism[20] is considered in this investigation, which includes the processes of direct electron impact ionization, electron attachment, electron–ion recombination, and photoionization.

The relevant reactions are listed in Table 2. Thus, the source term S_e in Eq. (1) and S_i in Eq. (3) could be computed with the following formula:

$$S_e = S_i = (\alpha - \eta)\mu_e |\boldsymbol{E}| n_e - \beta n_e n_p, \tag{6}$$

where the symbols α, η, and β represent the Townsend ionization coefficient, attachment coefficient, and recombination coefficient, respectively. n_p is the positive ion density. Although all the specifics of plasma composition cannot be explicitly described by using simplified chemistry, it is adequate to capture the essential elements of the discharge behavior. With the local field approximation, the transport properties of the gas are determined by the reduced electric field $|\boldsymbol{E}|/N$. The expressions of Townsend ionization coefficient, attachment coefficient, recombination coefficient, electron mobility, and electron diffusion coefficient adopted here are identical to those in Refs. [20,21], as follows:

$$\begin{aligned}
\alpha/N &= \begin{cases} 2.0\times10^{-20}\exp\left(\dfrac{-7.248\times10^{-19}}{|\boldsymbol{E}|/N}\right)\ \mathrm{m}^2, & |\boldsymbol{E}|/N > 1.5\times10^{-19}\ \mathrm{V\cdot m^2}, \\ 6.619\times10^{-21}\exp\left(\dfrac{-5.593\times10^{-19}}{|\boldsymbol{E}|/N}\right)\ \mathrm{m}^2, & |\boldsymbol{E}|/N \le 1.5\times10^{-19}\ \mathrm{V\cdot m^2}, \end{cases} \\
\eta/N &= \begin{cases} 8.889\times10^{-9}(|\boldsymbol{E}|/N) + 2.567\times10^{-23}\ \mathrm{m}^2, & |\boldsymbol{E}|/N > 1.5\times10^{-19}\ \mathrm{V\cdot m^2}, \\ 6.089\times10^{-9}(|\boldsymbol{E}|/N) - 2.893\times10^{-23}\ \mathrm{m}^2, & |\boldsymbol{E}|/N \ge 1.5\times10^{-19}\ \mathrm{V\cdot m^2}, \end{cases} \\
\beta &= 2.0\times10^{-13}\ \mathrm{m^{-3}\cdot s^{-1}}, \quad \mu_e = 2.3987|\boldsymbol{E}|^{-0.26}\ \mathrm{m^2\cdot V^{-1}\cdot s^{-1}}, \quad D_e = 4.3628\times10^{-3}|\boldsymbol{E}|^{0.22}\ \mathrm{m^2\cdot s^{-1}}.
\end{aligned} \tag{7}$$

Here $|\boldsymbol{E}|$ is the electric field strength in units $\mathrm{V\cdot m^{-1}}$, N is the number density of the background gas in units $\mathrm{m^{-3}}$.

Table 2. Reactions in gas phase included in the model. The symbols A and γ denote air and photons, respectively.

Index	Reaction	Rate coefficient
(R1)	$A + e \rightarrow A^+ + 2e$	α
(R2)	$A + e \rightarrow A^-$	η
(R3)	$A^+ + e \rightarrow A$	β
(R4)	$\gamma + A \rightarrow A^+ + e$	three-exponential Helmholtz model

For the photoionization in air, the three-exponential Helmholtz model derived by Luque *et al.*[22] is used. The photoionization source term, which results from the photoionization process of O_2 through the UV radiation from N_2 excited molecules, is given by

$$S_{ph} = \sum_{j=1}^{3} S_{ph}^{j}(r,t) \tag{8}$$

with terms $S_{ph}^{j}(r,t)$ obtained from the Helmholtz differential equations

$$\nabla^2 S_{ph}^{j}(r,t) - (\lambda_j p_{O_2})^2 S_{ph}^{j}(r,t) = -A_j p_{O_2}^2 I(r,t), \tag{9}$$

where $p_{O_2} = 150$ Torr (1 Torr = 1.33322×10^2 Pa) is the partial pressure of O_2 molecules at atmospheric pressure. λ_j and A_j are fitted coefficients calculated by Bourdon *et al.*[23] $I(r,t)$ is the radiation intensity, which is related to the electron ionization source term. It can be written in the form

$$I(r,t) = \frac{p_q}{p + p_q}\xi S_e, \tag{10}$$

where ξ represents the photoionization efficiency, p and p_q are the gas pressure and quenching pressure, respectively.

For initial conditions, a small quasi-neutral plasma spot is assumed at the tips of needles to save computational cost. The initial electron and positive ion densities are of a Gaussian distribution in the x and y directions, and are expressed as

$$\begin{aligned}
n_{e,\mathrm{initial}} &= n_{i,\mathrm{initial}} \\
&= n_{\max} \times \exp\left[-\frac{(x-x_0)^2}{Q_x^2} - \frac{(y-y_0)^2}{Q_y^2}\right] + n_0,
\end{aligned} \tag{11}$$

where $n_{\max} = 1\times10^{14}\ \mathrm{cm^{-3}}$ is the maximal density, x_0 and y_0 indicate the location of the needle tip, $Q_x = Q_y = 0.02$ cm. n_0 is the density of background charged species, defined as the remaining charges left after the previous discharge period. In this model, the background density is considered to be uniform as $10^9\ \mathrm{m^{-3}}$.

By using a finite element approach, the governing equations (Eqs. (1)–(3) and (5)) of the plasma dynamics model and the Helmholtz differential equations (Eqs. (8) and (9)) of the photoionization model are solved simultaneously in COMSOL 5.2a. To address the lack of a dedicated photoionization module in COMSOL 5.2a, a coupled modeling approach is implemented: the plasma fluid equations are solved using the DC Discharge interface within the Plasma Module, while the photoionization mechanism is incorporated by solving the Helmholtz equations configured via the Mathematics Module (Classical PEDs–Helmholtz equation interface). Specifically, the electron impact ionization source term computed by the

plasma module is passed as an input to the Helmholtz equation interface, whose solution yields the corresponding photoionization source S_{ph}. This photoionization source is then returned to the plasma module to self-consistently influence the discharge evolution. Through this bidirectional coupling between modules, the photoionization process is effectively integrated into the model. Triangular and mapped finite elements are employed. Local mesh refinement is implemented in the discharge channel region, particularly near the electrode surface, while a conventional coarser mesh is adopted in the other region to reduce computational costs. The refined mesh for the case of $L = 2$ cm ($x < 2.5$ cm) is shown in Fig. 2; the coarse mesh outside this region is omitted for clarity. The minimum mesh size is 0.012 mm, and nearly 1.5×10^5 elements are employed. The average computational time required to obtain the results for one calculation (2 ns) is about two days on an HP Z238 station.

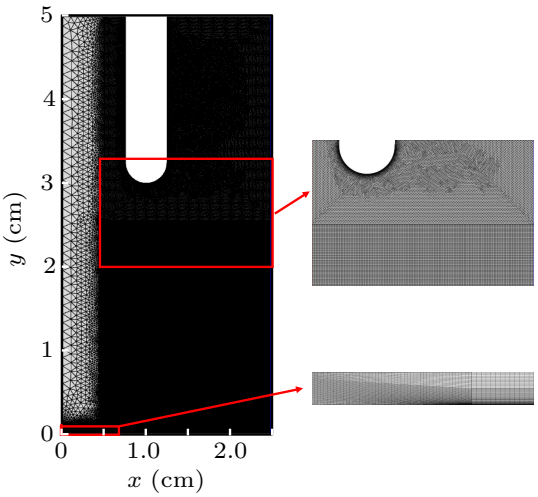


Fig. 2. The mesh configuration for the region where $x < 2.5$ cm. The inset provides a detailed view of the discharge channel and electrode surface.

3. Results and discussion

3.1. Benchmark of photoionization model

To confirm the validity and the applicability of photoionization source S_{ph} obtained by three-exponential Helmholtz model, a simple photoionization model is utilized to compute the photoionization source under comparable conditions as in previous study.[23] According to Bourdon *et al.*,[23] the ionization source S_i is considered to have a Gaussian distribution. Figures 3(a) and 3(b) depict the test outcomes obtained with Sommerfeld's radiation boundary condition. The axial and radial profiles of the photoionization source term S_{ph} illustrated in figure exhibit an excellent match with the results of Bourdon *et al.*[23] Given the foregoing, the validity and the applicability of the three-exponential Helmholtz model for photoionization are validated.

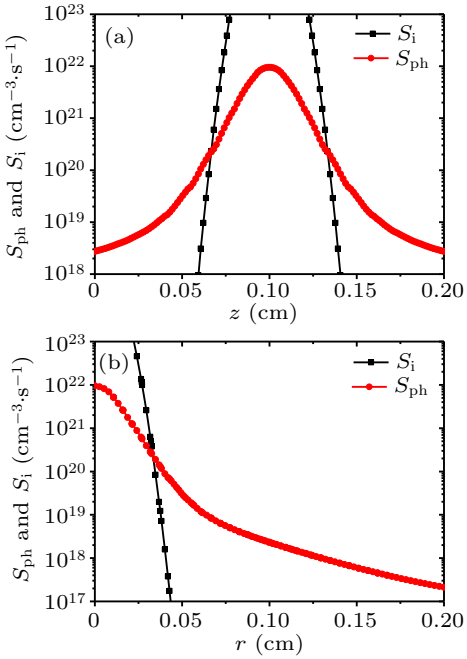


Fig. 3. Axial (a) and radial (b) profiles of the ionization source term S_i and the photoionization source term S_{ph} of the three-exponential Helmholtz model.

3.2. Discharge dynamics for a twin needle electrode configuration

As a point of departure, the discharge dynamics of plasma generated by a twin needle electrode configuration with a spacing between needles of 2 mm are explored. Figure 4 plots the spatial distribution of electron density and electric field at moments $t = 0.5$, 1.0, 1.5, and 2.0 ns. When the voltage is supplied, two positive discharge filaments are ignited simultaneously in the vicinity of the needle tips and spread equally quickly between the needle electrode and grounded electrode. At $t = 0.5$ ns, the peak maximum electron density is formed at the tip of the needle, and the peak electric field is located on the front of the discharge. From 0.5 ns to 1.0 ns, the peak electric field and electron density in the discharge front progressively decline as the discharge leaves the needle tips. As the discharge approaches the grounded electrode, the discharge intensity increases somewhat on the surface of the grounded electrode.

These simulation results show good consistency with the experimental observations reported by Yang *et al.*[17] for a comparable electrode arrangement. This correspondence is particularly meaningful given the different cathode configurations — our model uses a bare metal cathode while their experiment employed a dielectric-covered electrode. The observed agreement confirms that the early development and propagation path of the discharge is primarily determined by gas-phase mechanisms, specifically electric field enhancement and photoionization processes ahead of the streamer front, with minimal influence from cathode surface characteristics during this initial phase. This interpretation is supported by our earlier

investigations.[18,24] As anticipated, differences emerge during the final attachment stage. While the discharge spreads across the dielectric surface in Yang *et al.*'s experiment, our simulation shows a concentrated, high-intensity attachment point forming on the metal cathode. This localized attachment behavior on metallic substrates aligns well with both the experimental data from Pei *et al.*[25] and numerical simulations by Zhang *et al.*[16]

It is well known that the interaction of discharge arrays depends on electrostatic repulsion and attraction caused by non-local photoionization.[14] To provide further context for the discharge behavior shown in Fig. 4, the spatial distributions of the photoionization source $S_{\rm ph}$ and the net space charge density are plotted on a log scale in Fig. 5.

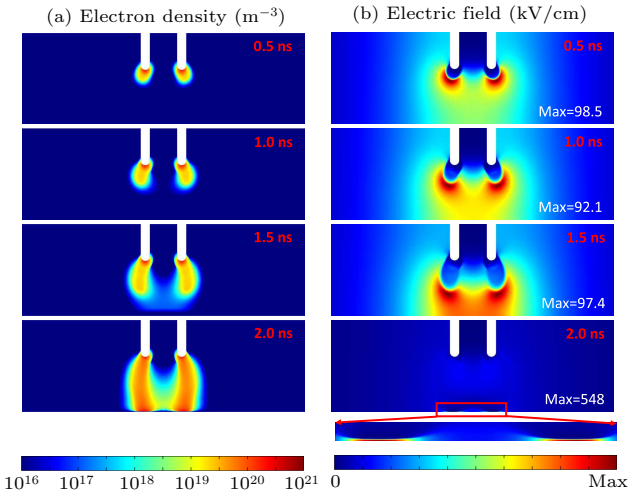


Fig. 4. Spatial profiles of (a) electron density and (b) electric field at $t = 0.5$, 1.0, 1.5, and 2.0 ns. The electric field near the cathode at $t = 2.0$ ns is expanded for better visualization.

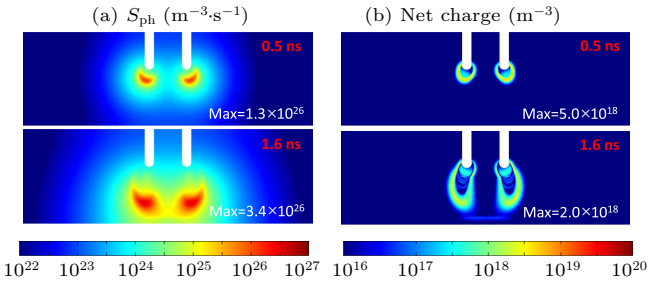


Fig. 5. Spatial profiles of (a) photoionization source and (b) net space charge density at $t = 0.5$ ns and 1.6 ns. The maximum values in the discharge front are shown in the corresponding frame.

As expected, the maximum photoionization source is located on the discharge front, where the ionization source has a local maximum. Due to positive polarity, the discharges have a positive space charge in the discharge front. Obviously, the discharge fronts can interact through attraction due to non-local photoionization and Coulomb repulsive force created by a space charge of the same polarity. The discharges initially resist each other, as illustrated in Fig. 4, suggesting that the mutual repulsion force outweighs the mutual attraction. From 0.5 ns to 1.6 ns, the peak value of the photoionization source increases, resulting in an increase in the mutual attraction between discharge fronts. Meanwhile, the electrostatic repulsion force is weakening as the peak net charge density in discharge front decreases. As a result, the distance between discharge propagation paths shrinks somewhat as discharge fronts approach to the plate electrode.

It is widely recognized that photoionization is crucial for gas discharge processes. A quantitative comparison between photoionization and direct electron impact ionization is essential to clarify their relative contributions. To address this point, Fig. 6 shows the spatiotemporal distributions of both the photoionization source and the direct electron impact ionization source. It can be observed that although the peak value of the direct electron impact ionization rate is larger than that of photoionization at the discharge fronts, photoionization becomes the dominant ionization mechanism in regions away from the primary ionization zone. Specifically, the photoionization source is stronger in areas such as the interspace between two discharge channels and in the regions ahead of the discharge fronts. Given that the initial background seed electron density was only on the order of 10^9 m^{-3}, a value too low for efficient propagation, this distributed photoionization plays a critical role, particularly during the initial stage. It ensures a sufficient supply of seed electrons in otherwise low-electron-density regions, thereby effectively sustaining the inception and subsequent development of the discharge.

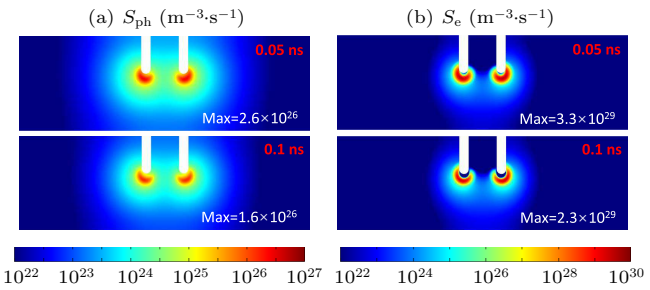


Fig. 6. Spatial profiles of (a) photoionization source and (b) source of direct electron impact ionization at $t = 0.05$ ns and 0.1 ns. The maximum values in the discharge front are shown in the corresponding frame.

3.3. Influencing factors of discharge behaviors

It has been reported that the characteristics of discharge in the needle arrays are sensitive functions of the discharge parameters.[12,17] In this section, the influence of spacing between needle electrodes, pulsed peak voltage, pulse polarity on the discharge development and homogeneity is explored.

To begin, discharges from a single electrode and double-needle electrodes with spacing of 1 mm, 6 mm, and 10 mm are purposefully chosen to evaluate the effect of needle spacing on discharge dynamics. Figure 7 depicts a comparison of the spatial distributions of electron density at $t = 1.5$ ns and 2.0 ns. The first observation is that the needle spacing affects the interaction of two concurrently propagating discharges. The discharge development exhibits a trend similar to the baseline

($L = 2$ mm) even with reduced needle spacing ($L = 1$ mm). Due to competition between electrostatic repulsion and attraction, the two discharges first repel each other before attracting each other. With an increase in needle spacing, the propagation route switches from a curved trajectory with 1-mm and 2-mm needle spacing to a nearly straight-line trajectory with 10-mm separation, the latter being similar to that of the single needle case. The electron density distribution and propagation path for a single needle exhibit a symmetric structure about the needle axis. This suggests that the interaction between two discharges diminishes with increasing needle separation, and becomes negligible at 10-mm needle spacing. Another finding concerns the propagation velocity: in comparison to the single-needle case, the propagation is slower in double-needle configurations due to mutual interaction; however, within the double-needle configuration, the velocity increases with larger needle spacing, as shown in Fig. 7(a), owing to the weaker interaction. This outcome is in accordance with the findings of Naidis.[13]

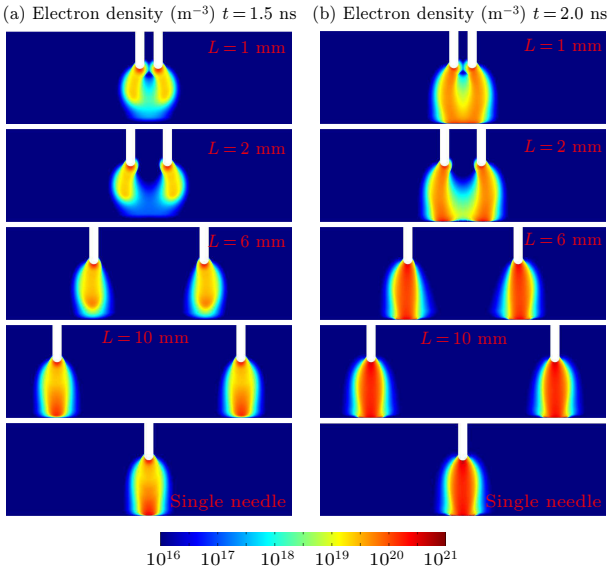


Fig. 7. Spatial profiles of electron density for double needle electrodes with separations of 1, 2, 5, and 10 mm, compared with the case of a single needle electrode, at (a) 1.5 ns and (b) 2.0 ns.

The variation in the needle spacing significantly alters the Laplace field distribution, which is crucial to the discharge characteristics. To investigate how the Laplace electric field affects the discharge behaviors, the spatial profiles of Laplace electric field (*i.e.*, electric field at $t = 0$ ns) for varying needle–needle spacing, compared with the case of a single-needle electrode are given in Fig. 8. In contrast to the symmetric field distribution of the single-needle case, the double-needle configurations exhibit clear field distortion due to electrostatic repulsion between adjacent needle tips. This distortion is most pronounced at small spacings ($L = 1$ mm) and progressively diminishes with increasing separation. At 10 mm spacing, the field distribution becomes nearly axisymmetric and closely resembles that of the single-needle case, with comparable peak field strengths, indicating negligible interaction at this distance. This field distortion directly explains the observed discharge behavior. While single-needle discharges develop symmetrically, double-needle configurations show curved propagation paths and asymmetric electron density distributions due to mutual interaction. The field distortion also accounts for the reduced propagation velocity in double-needle setups compared to the single-needle case, as energy is diverted into lateral interactions. Meanwhile, within double-needle configurations, larger spacing (from 1 mm to 10 mm) yields higher maximum electric fields (141 kV/cm to 164 kV/cm) at the needle tips, resulting in increased propagation velocity and peak electron density as the interaction weakens. These findings demonstrate that needle spacing controls discharge characteristics through its direct influence on the initial Laplace field distribution.

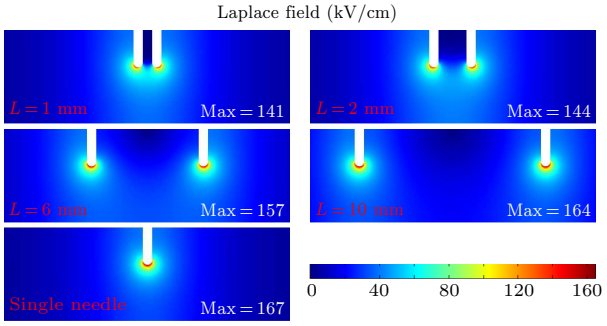


Fig. 8. Spatial profiles of Laplace field for double needle electrodes with separations of 1, 2, 5, and 10 mm, compared with the case of a single needle electrode.

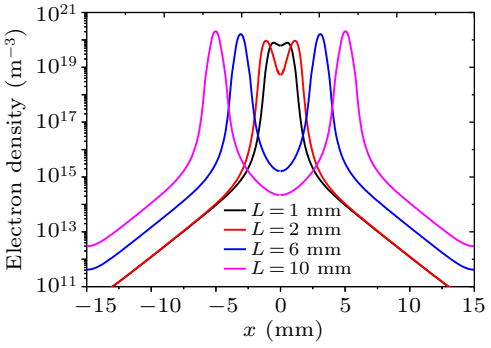


Fig. 9. The horizontal distribution of electron density at a position 2 mm above the plate electrode for varied needle to needle spacing.

To further explore the impact of needle spacing on discharge uniformity, the horizontal profiles of electron density at a position 2 mm above the surface of the plate electrode for varied needle-to-needle spacing are given in Fig. 9. The profiles are clearly seen to have a ring-shaped structure. This finding appears to be in good accord with experimental results by Yang *et al.*[17] The peak of electron density is located off axis at a distance that increases with needle separation. As the needle spacing rises, the electron density at the center ($x = 0$) falls fast, while the maximum electron density slightly increases. A homogeneity coefficient, denoted as K, is introduced to quantitatively evaluate the spatial uniformity of the discharge. This

coefficient is defined as the ratio of the peak electron density to the electron density at the central axis (*i.e.*, at $x = 0$). A value of K closer to 1 indicates a more uniform distribution. The calculated K increases from 1.3×10^5 to 9.5×10^5 as the needle spacing rises from 1 mm to 10 mm, confirming that spatial homogeneity decreases with increasing needle spacing.

Moreover, we perform simulations to investigate how the applied voltage amplitude affects discharge behavior. Figure 10 shows the temporal-spatial distributions of electron density under pulse peak voltages of 15 kV, 16 kV, and 17 kV. It is clearly demonstrated that as the applied voltage amplitude increases, so do the discharge intensity and propagation velocity. These variances in discharge behavior are caused by different Laplacian electric fields established in the discharge gap. The Laplacian electric field in the discharge gap grows when the applied voltage amplitude increases from 15 kV to 17 kV, resulting in more energy dissipated into the plasma. Thus, the discharge intensity is enhanced with increasing applied voltage amplitude. In addition, variation of the applied voltage amplitude affects the discharge uniformity.

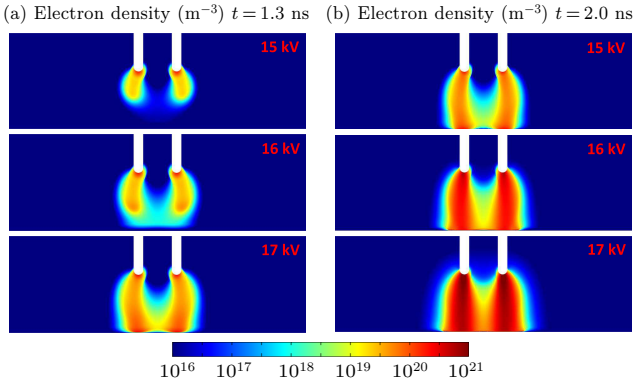


Fig. 10. Spatial profiles of electron density at (a) 1.3 ns and (b) 2.0 ns for double needle electrodes under the pulsed peak voltage of 15, 16, and 17 kV.

For more quantitative comparisons, the horizontal profiles of electron density at a position 2 mm above the surface of the plate electrode for various pulse peak voltages are plotted in Fig. 11. As shown, the plasma volume in the horizontal direction is enlarged as the voltage amplitude applied increases. Meanwhile, the coefficient K drops from 17.4 to 12.6 as the voltage rises from 15 kV to 17 kV, providing quantitative evidence that a higher operating voltage promotes a more uniform discharge.

Finally, the influence of voltage polarity on discharge dynamics is examined. A negative polarity voltage of the same amplitude is supplied to the needle electrodes. Figure 12 shows the temporal-spatial distributions of electron density and electron impact ionization source. A comparison of electron density for positive and negative polarities reveals that the polarity of pulse voltage affects the discharge evolution. The discharges are more diffusive, and the discharge channels are wider under the negative polarity. In comparison to positive discharges, negative discharges propagate more quickly. Negative discharges have an earlier impact on the plate electrode. A similar polarity effect of applied voltage on discharge propagation has been observed in experimental studies by Beloplotov *et al.*[26] and Wang *et al.*[27] In the study of Beloplotov *et al.*,[26] pre-ionization of the gas in the discharge gap as a result of the generation of runaway electrons for negative polarity is thought to be a contributing element to the variation in propagation velocities. Upon impact on the plate electrode, a conductive channel is established between the needle electrodes and the plate electrode. Electron impact ionization occurs throughout the conductive channel, producing a higher electron density for the negative polarity.

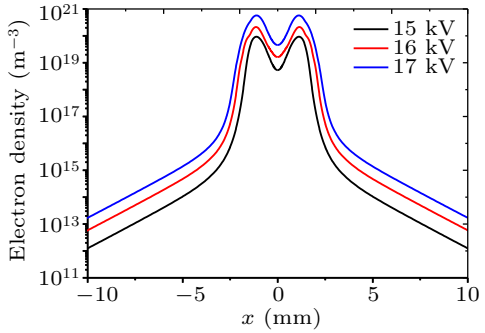


Fig. 11. The horizontal distribution of electron density at a position 2 mm above the plate electrode for different voltage amplitude applied.

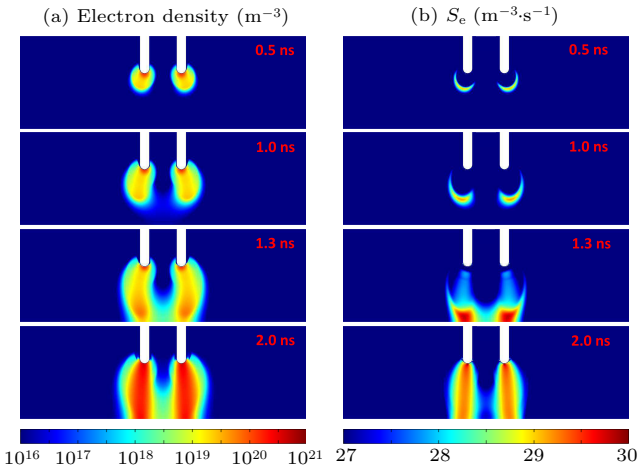


Fig. 12. Spatial profiles of (a) electron density and (b) electron impact ionization source (plotted on a log scale) at $t = 0.5$, 1.0, 1.3, and 2.0 ns for a negative voltage −15 kV.

The observed higher propagation velocity of the negative polarity, compared to the positive one, can be attributed to the distinct properties of its ionization front. While pre-ionization by runaway electrons may play a role in practice, our fluid model reveals that the difference emerges naturally from the fundamental electrodynamics. To elucidate this, Fig. 13 compares the spatial distribution of the ionization frequency and net space charge density at the moment the discharges have propagated to the same position. These two parameters are critical factors governing streamer propagation velocity.[28,29]

As evident from Fig. 13(a), the negative discharge exhibits a peak ionization frequency that is substantially higher than that of the positive streamer. Furthermore, Fig. 13(b) shows that the spatial extent (the scale) of the space charge layer driving the field distortion is larger for the negative polarity. A larger, more intense space charge layer leads to a stronger electric field enhancement ahead of the streamer, which in turn accelerates electrons more effectively and fuels a more rapid avalanche. The combination of a higher peak ionization frequency and a broader space charge layer provides a self-consistent explanation for the faster propagation of the negative discharge.

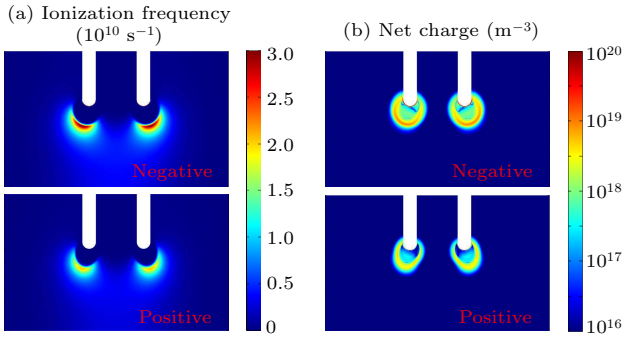


Fig. 13. Comparative analysis of discharge front dynamics for positive and negative polarities at an identical propagation distance. Spatial distribution of (a) ionization frequency, (b) the net space charge density.

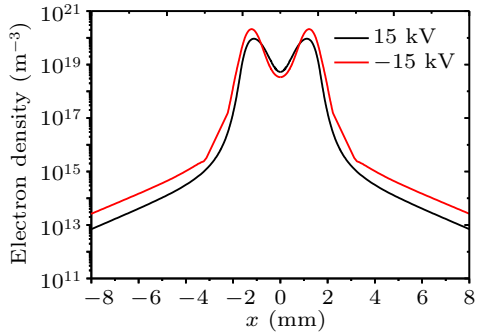


Fig. 14. Horizontal profiles of electron density at a position 2 mm above the plate electrode for positive and negative voltage polarities.

Figure 14 shows the polarity effect on discharge structure and uniformity. The discharge polarity has no effect on the ring-shaped distribution, but it does alter the discharge uniformity. The peak electron density in the discharge channel is observed to be larger, while the electron density in the region between two discharge channels ($x = 0$) is lower for negative polarity than that for positive polarity. The calculated K for the negative polarity discharge is 62.8, which is notably higher than the value of 17.4 for the positive polarity. This quantitatively confirms that the positive discharge, under these conditions, yields a more homogeneous plasma structure despite the negative discharge covering a broader area. The reason for the reduction in the uniformity of the negative discharge is a larger electrostatic repulsive force between discharge fronts with increased ionization intensity.

4. Conclusions

Based on a 2D fluid model, a numerical investigation of atmospheric pressure discharge using two-needle array-plane electrode in air has been performed. Three-exponential Helmholtz models for photoionization in air were considered in the fluid model. Emphasis was placed on the effect of the discharge parameters (needle to needle spacing, pulsed peak voltage, and voltage polarity) on the spatial scale and uniformity of the discharge array. Two identical discharges were initiated at the tips of the array needle electrode, then simultaneously propagated towards the plane electrode along curved trajectories at the same speed. The distance between the two discharge fronts first increased and then decreased as a result of the balance between the attractive term and the electrostatic repulsive term. By increasing the spacing between needles, or the pulse peak voltage, the discharge was strengthened due to the enhancement of the Laplacian electric field. Larger-scale plasma can be created by increasing needle spacing or increasing the pulse peak voltage. In contrast to positive polarity, negative polarity discharges are broader and more diffuse. The discharge homogeneity is a sensitive function of the spacing between needles, pulse peak voltage, and voltage polarity, as quantitatively demonstrated by the coefficient K. It is conclusively shown that smaller needle spacing (K decreases from 9.5×10^5 to 1.3) and greater peak voltage (K decreases from 17.4 to 12.6) result in more homogeneous discharge structures. In comparison to negative polarity ($K = 12.6$), the discharge for positive polarity ($K = 17.4$) is quantitatively more homogeneous.

Acknowledgements

Project supported by National Natural Science Foundation of China (Grant No. 11705022 and 12375198), the Liaoning Provincial Science and Technology Program (Grant Nos. 2024JH/102600109 and 2023JH2/101700307), and the National College Students Innovation and Entrepreneurship Training Program (Grant No. 202512026068).

References

[1] Adamovich I, Agarwal S, Ahedo E, *et al.* T 2022 *J. Phys. D: Appl. Phys.* **55** 373001 (55pp)
[2] Lu X P, Bruggeman P J, Reuter S, Naidis G, Bogaerts A, Laroussi M, Keidar M, Robert E, Pouvesle J M, Liu D W and Ostrikov K 2022 *Front. Phys.* **10** 1
[3] Nau-Hix C, Holsen T M and Mededovic Thagard S 2022 *Plasma Process. Polym.* **19** 1
[4] Zhou R, Zhou R, Wang P, Xian Y, Mai-Prochnow A, Lu X, Cullen P J, Ostrikov K, Ken O and Bazaka K 2020 *J. Phys. D: Appl. Phys.* **53** 303001
[5] Ulrich K 2003 *Plasma Chem. Plasma Process.* **23** 1
[6] Lu X, Laroussi M and Puech V 2012 *Plasma Sources Sci. Technol.* **21** 34005
[7] Bruggeman P J, Kushner M J, Locke B R, *et al.* 2016 *Plasma Sources Sci. Technol.* **25** 53002
[8] Pai D Z, Lacoste D A and Laux C O 2010 *Plasma Sources Sci. Technol.* **19** 65015

[9] Liu Z, Wang W, Yang D, Wang S, Zhang S, Tang K and Jiang P 2014 *Spectrochim. ACTA PART A Mol. Biomol. Spectrosc.* **121** 698

[10] Zhang L, Yang D, Wang W, Liu Z, Wang S, Jiang P, Zhang S, Zhang L, Yang D, Wang W, Liu Z, Wang S and Jiang P 2014 *J. Appl. Phys.* **116** 113301

[11] Liu Z, Wang W, Zhang L, Wang S, Yang D, Zhang S, Tang K, Liu Z, Wang W, Zhang L, Wang S, Yang D and Zhang S 2014 *J. Appl. Phys.* **115** 203302

[12] Gu J, Zhang C, Wang R, Yan P and Shao T 2016 *Plasma Sci. Technol.* **18** 230

[13] Babaeva N Y, Naidis G V, Naidis G V and Naidis G V 1996 *J. Phys. D: Appl. Phys.* **29** 779

[14] Luque A, Ebert U and Hundsdorfer W 2008 *Phys. Rev. Lett.* **101** 75005

[15] Massot M 2012 *Plasma Sources Sci. Technol.* **21** 52001

[16] Zhang J, Wang Y and Wang D 2018 *Phys. Plasmas* **25** 72101

[17] Yang D, Wang W, Jia L, Nie D, Shi H, Yang D, Wang W, Jia L, Nie D and Shi H 2011 *J. Appl. Phys.* **109** 73308

[18] Yan W and Economou D J 2016 *J. Appl. Phys.* **120** 123304

[19] Yan W, Xia Y, Bi Z, Song Y, Wang D, Sosnin E A and Liu D 2017 *J. Phys. D: Appl. Phys.* **50** 345201

[20] Bagheri B and Teunissen J 2019 *Plasma Sources Sci. Technol.* **28** 45013

[21] Morrow R and Lowke J J 1997 *J. Phys. D: Appl. Phys.* **30** 614

[22] Luque A, Ebert U, Montijn C and Hundsdorfer W 2007 *Appl. Phys. Lett.* **90** 81501

[23] Bourdon A 2007 *Plasma Sources Sci. Technol.* **16** 656

[24] Yan W and Economou D J 2017 *J. Phys. D: Appl. Phys.* **50** 415205

[25] Pei X, Wang Z, Huang Q, Wu S and Lu X 2011 *IEEE Trans. Plasma Sci.* **39** 2276

[26] Beloplotov D V, Genin D E and Pechenitsin D S 2020 *Jpn. J. Appl. Phys.* **59** SHHC06

[27] Wang D, Namihira T and Akiyama H 2011 *J. Adv. Oxid. Technol.* **14** 131

[28] Wu S, Lu X, Yue Y, Dong X and Pei X 2016 *Phys. Plasmas* **23** 103506

[29] Kulikovsky A A 1998 *Phys. Rev. E* **57** 7066